Chapter 6

Electron Beam-Induced Directional Terahertz Radiation from Metamaterials

Tatsunosuke Matsui

Additional information is available at the end of the chapter

http://dx.doi.org/10.5772/intechopen.80648

Abstract

We have numerically analyzed an electron beam (e-beam)-induced directional terahertz (THz) radiation from metamaterials. Here, we used metallic grating structures with graded depths, in which only one-way surface mode can be supported based on the spoof surface plasmon polariton (spoof SPP) concept and gives unique directional THz radiation. For numerical analysis, we used a simplified particle-in-cell (PIC) finite-difference time-domain (FDTD) method. First, we describe our simplified PIC-FDTD method in detail. Then, we show our results on the e-beam-induced directional THz radiation from graded grating with graded depths. By passing pulsed (bunched) e-beam along the grating surface, directional THz radiations are obtained from one side of the grating with shallower grooves. The direction of these radiations can be switched backward or forward by making the groove depth deeper or shallower. The spectra of these directional radiations are wideband and contain multiple sharp peaks. The deepest and the shallowest groove depths determine the lowest and the highest frequency of the radiation band, respectively. These unique radiation characteristics cannot be explained by the conventional Smith-Purcell radiation and should be attributed to the spoof SPP that originates from different locations on the graded grating.

Keywords: metamaterial, graded grating, electron beam, terahertz, THz, Smith-Purcell radiation, particle-in-cell finite-difference time-domain, PIC-FDTD

1. Introduction

Recently, terahertz (THz) science and technology have been extensively studied from various viewpoints [1, 2]. The THz frequency range is generally considered to be the range of 0.1–10 THz. The electromagnetic (EM) waves that fall in the THz range can be utilized for various types of applications such as spectroscopy, nondestructive inspection, security, and information

and communications technology. Optical techniques for a generation and detection of the THz radiation usually require ultrafast short-pulsed lasers. As an alternative way, vacuum electronic-based techniques have attracted much attention to develop next-generation table-top THz radiation sources [3]. It has been known as Smith-Purcell radiation (SPR) since the 1950s that EM radiation can be obtained by passing electron beam (e-beam) accelerated at a relativistic speed along the surface of periodically corrugated metallic grating [4]. The wavelength λ_{SPR} and the radiation angle θ_{SPR} of SPR measured from the direction of the e-beam satisfy the following simple relation:

$$\lambda_{SPR} = \frac{\Lambda}{|n|}\left(\frac{1}{\beta} - \cos\theta_{SPR}\right) \tag{1}$$

where Λ is the period of the grating, βc is the electron velocity, c is the speed of light in vacuum, and integer n is the order. Therefore, one can choose any spectral range of EM radiation in principle by appropriately designing the grating period Λ. The original type of SPR is not efficient enough to be widely utilized; however, there has been renewed interest in this area of research since the observation of superradiance by Urata et al. in 1998 [5]. They used an electron gun in a scanning electron microscope to flow a large current and discovered a nonlinearly growing radiation power (superradiance). Theoretical [6, 7] and numerical [8–10] investigations revealed that the bunching of an e-beam due to the interaction with induced surface waves on the grating was essential to achieve superradiance through intrabunch and interbunch double coherence. In such numerical investigations, the particle-in-cell finite-difference time-domain (PIC-FDTD) method has been widely employed to reproduce the Smith-Purcell superradiance.

On the other hand, quite significant progress has been made in the researches on metamaterials in recent years, and various novel optical effects have been proposed and demonstrated, such as negative refraction, superlensing, and optical cloakings [11–13]. Based on metamaterials' concept, one can design a rich variety of optical materials with unique dispersion characters which cannot be obtained in nature. The metamaterials' concept also offers new designing freedom of surface waves. It has been believed that surface waves like surface plasmon polaritons (SPPs) in the visible or near infrared cannot be supported in longer wavelength range like in THz because metals tend to behave as a perfect electric conductor (PEC). However, Pendry et al. showed that surface waves like SPPs could be supported even on PECs provided that there were arrays of corrugations or holes on metals [14, 15]. The dispersion relations of such surface waves resemble those of SPPs, and the surface waves introduced by Pendry et al. are usually called *spoof SPPs*. Dispersion relations of the spoof SPPs strongly depend on the dimensions of corrugations and holes, which in turn implies that almost arbitrary dispersion relations for the spoof SPPs can be designed through an appropriate choice of structural parameters. Based on this concept, Gan et al. demonstrated an ultrawide-bandwidth slow-light system with a graded metallic grating with linearly graded depths [16]. Since the dispersion of the spoof SPPs is strongly dependent on the geometrical parameters of the grooves, the upper limit (cutoff) frequencies for the existence of spoof SPPs are also determined by the groove geometries. The group velocity of each mode approaches zero near the cutoff frequency; therefore, graded grating structures with spatially varying dispersions are capable of stopping spoof SPPs with different frequencies at different locations

along the surface. The spatial distribution of spoof SPPs with different frequencies can be tuned by appropriately designing the grade of the grating depths.

Here, we show an e-beam-induced THz radiation from such graded grating based on PIC-FDTD method [3, 17]. We have obtained THz radiation with unique characteristics such as arbitrarily chosen bandwidth and unique directionality, which cannot be expected from the conventional theory developed for the SPR. Our findings may be utilized to develop novel e-beam-based THz radiation sources.

2. Numerical simulation

In this section, numerical simulation techniques employed in this study, simplified PIC-FDTD method, is described in detail, and parameters for our simulations are summarized.

2.1. Overview of simplified PIC-FDTD approach for the analysis of e-beam-induced THz radiation

The PIC-FDTD method has been widely used to study underlying physical mechanism of the Smith-Purcell superradiance [8–10]. To save computational time and memory, we have used simplified version of PIC-FDTD method [17, 18]. In our simplified model, the electron-bunch is treated as one negatively charged particle, the movement of the particle is restricted only in two-dimensional (2D) (x-y) plane, and only transverse electric (TE) mode, with E_x, E_y, and H_z fields, has been analyzed. **Figure 1** shows schematic representation of the analyzed 2D system and definitions of dimensions of the graded grating, where Λ, s, d, and Δd are period, width, depth of the grooves, and depth variation, respectively.

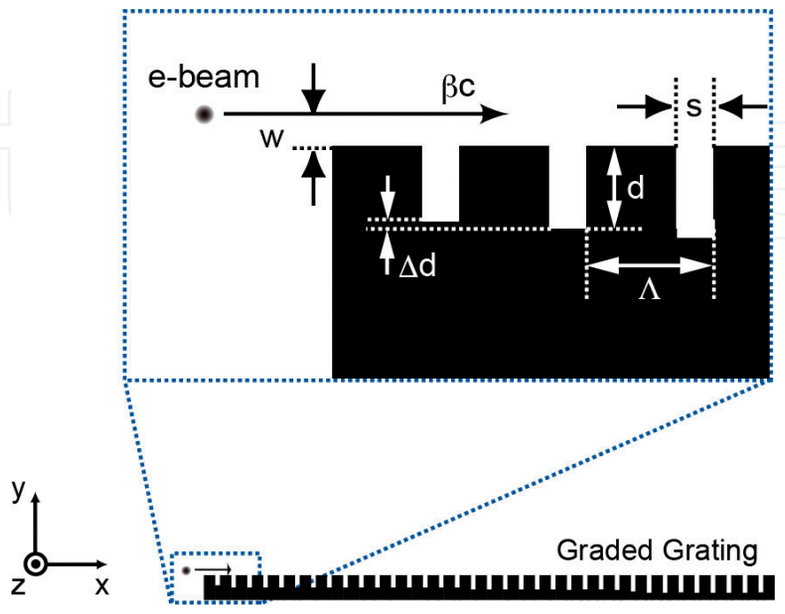

Figure 1. Schematic representation of the analyzed 2D system and definitions of dimensions of the graded grating.

In the FDTD method, the time-dependent EM field propagating in 2D system is simulated using Yee's algorithm [19, 20] to solve the following Maxwell's equations (in the vacuum):

$$\nabla \times \boldsymbol{E}(x,y,t) = -\frac{\partial \boldsymbol{B}(x,y,t)}{\partial t} \tag{2}$$

$$\nabla \times \boldsymbol{H}(x,y,t) = \varepsilon_0 \frac{\partial \boldsymbol{E}(x,y,t)}{\partial t} + \boldsymbol{J}(x,y,t) \tag{3}$$

where $\boldsymbol{E}$, $\boldsymbol{H}$, and $\boldsymbol{B}$ are the electric and magnetic fields and magnetic flux density of EM wave, $\boldsymbol{J}$ is the current density, and ε_0 and μ_0 are the dielectric permittivity and the magnetic permeability in vacuum, respectively. In Yee's algorithm, these differential equations are discretized using centered finite-difference expressions for the space and time derivatives, and we have the following set of equations for TE mode in 2D space:

$$E_x^n\left(i+\frac{1}{2},j\right) = C_{EX}\left(i+\frac{1}{2},j\right)E_x^{n-1}\left(i+\frac{1}{2},j\right) + C_{EXLY}\left(i+\frac{1}{2},j\right)\left\{H_z^{n-\frac{1}{2}}\left(i+\frac{1}{2},j+\frac{1}{2}\right) - H_z^{n-\frac{1}{2}}\left(i+\frac{1}{2},j-\frac{1}{2}\right)\right\} \tag{4}$$

$$E_y^n\left(i,j+\frac{1}{2}\right) = C_{EY}\left(i,j+\frac{1}{2}\right)E_y^{n-1}\left(i,j+\frac{1}{2}\right) + C_{EYLX}\left(i,j+\frac{1}{2}\right)\left\{H_z^{n-\frac{1}{2}}\left(i+\frac{1}{2},j+\frac{1}{2}\right) - H_z^{n-\frac{1}{2}}\left(i-\frac{1}{2},j+\frac{1}{2}\right)\right\} \tag{5}$$

$$H_z^{n+\frac{1}{2}}\left(i+\frac{1}{2},j+\frac{1}{2}\right) = H_z^{n-\frac{1}{2}}\left(i+\frac{1}{2},j+\frac{1}{2}\right) - C_{HZLX}\left(i+\frac{1}{2},j+\frac{1}{2}\right)\left\{E_y^n\left(i+1,j+\frac{1}{2}\right) - E_y^n\left(i,j+\frac{1}{2}\right)\right\}$$

$$+C_{HZLY}\left(i+\frac{1}{2},j+\frac{1}{2}\right)\left\{E_x^n\left(i+\frac{1}{2},j+1\right) - E_x^n\left(i+\frac{1}{2},j\right)\right\} \tag{6}$$

where superscript n is for the time step and $(i, j) = (i\Delta x, j\Delta y)$ for the spatial position. The coefficients in Eqs. (4)–(6) are as follows:

$$C_{EX}\left(i+\frac{1}{2},j\right) = \frac{1-\frac{\sigma\left(i+\frac{1}{2},j\right)\Delta t}{2\varepsilon\left(i+\frac{1}{2},j\right)}}{1+\frac{\sigma\left(i+\frac{1}{2},j\right)\Delta t}{2\varepsilon\left(i+\frac{1}{2},j\right)}} \tag{7}$$

$$C_{EXLY}\left(i+\frac{1}{2},j\right) = \frac{\frac{\Delta t}{\varepsilon\left(i+\frac{1}{2},j\right)}}{1+\frac{\sigma\left(i+\frac{1}{2},j\right)\Delta t}{2\varepsilon\left(i+\frac{1}{2},j\right)}}\frac{1}{\Delta y} \tag{8}$$

$$C_{EY}\left(i,j+\frac{1}{2}\right) = \frac{1-\frac{\sigma\left(i,j+\frac{1}{2}\right)\Delta t}{2\varepsilon\left(i,j+\frac{1}{2}\right)}}{1+\frac{\sigma\left(i,j+\frac{1}{2}\right)\Delta t}{2\varepsilon\left(i,j+\frac{1}{2}\right)}} \tag{9}$$

$$C_{EYLX}\left(i,j+\frac{1}{2}\right) = \frac{\frac{\Delta t}{\varepsilon\left(i,j+\frac{1}{2}\right)}}{1+\frac{\sigma\left(i,j+\frac{1}{2}\right)\Delta t}{2\varepsilon\left(i,j+\frac{1}{2}\right)}}\frac{1}{\Delta x} \tag{10}$$

$$C_{HZLX}\left(i+\frac{1}{2},j+\frac{1}{2}\right)=\frac{\Delta t}{\mu\left(i+\frac{1}{2},j+\frac{1}{2}\right)}\frac{1}{\Delta x} \tag{11}$$

$$C_{HZLY}\left(i+\frac{1}{2},j+\frac{1}{2}\right)=\frac{\Delta t}{\mu\left(i+\frac{1}{2},j+\frac{1}{2}\right)}\frac{1}{\Delta y} \tag{12}$$

Figure 2 shows a typical Yee's 2D uniform rectangular grid for TE mode. E_x and E_y components are located at the middle of the edge of each grid, and H_z component is located at the center of the grids. The time evolution of EM fields is updated in a leapfrog manner. In order to model an open system, we have employed perfectly matched layer (PML)-absorbing conditions [21].

The dielectric properties of metals are strongly dispersive; therefore, we utilized recursive convolution (RC) approach [20] to model metallic grating. By adopting Drude model, frequency dependence of dielectric permittivity of metal can be expressed as follows:

$$\varepsilon_r(\omega)=1+\frac{\omega_p^2}{\omega(j\Gamma-\omega)}=1+\chi(\omega) \tag{13}$$

$$\chi(\omega)=\frac{\omega_p^2}{\omega(j\Gamma-\omega)} \tag{14}$$

where ω_p and Γ are the plasma frequency and collision frequency of metal, respectively. In a linear dispersive medium, the time-domain electric flux density $\boldsymbol{D}(t)$ is related to the electric field $\boldsymbol{E}(t)$ by the convolution:

$$\boldsymbol{D}(t)=\varepsilon_0\varepsilon_\infty\boldsymbol{E}(t)+\varepsilon_0\int_{\tau=0}^{t}\boldsymbol{E}(t-\tau)\chi(\tau)d\tau \tag{15}$$

Since the Fourier-transformed electric susceptibility $\chi(\tau)$ of Drude type of dispersion satisfies the condition for a recursive computation, the convolution in Eq. (15) can be solved in a recursive manner.

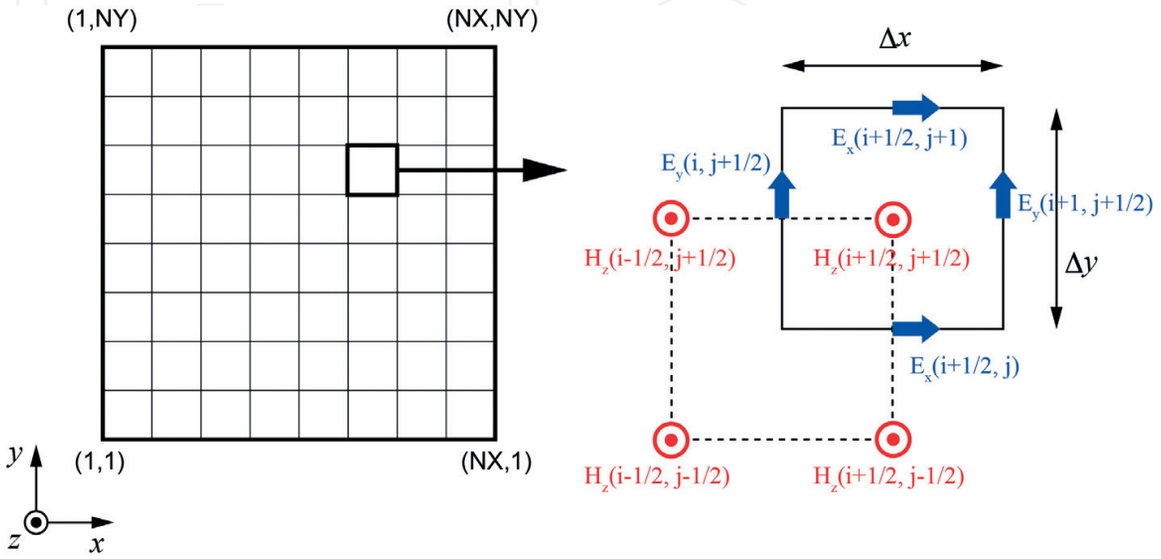

Figure 2. 2D uniform rectangular Yee's grid for TE mode.

In the PIC-FDTD method, time-dependent Maxwell's equations are coupled with the equation of motion of relativistic charged particles driven by the inertia and the Lorentz force and solved in a leapfrog manner similar to the main FDTD algorithm. In our simplified version, we assume the electron-bunch as one negatively charged particle with the following Gaussian spatial charge distribution:

$$n_e(x,y,t) = N_0 exp\left\{-\frac{(x-x_0(t))^2 + (y-y_0(t))^2}{2\sigma^2}\right\} \tag{16}$$

$$\sigma = \frac{w}{2\sqrt{2ln(2)}} \tag{17}$$

where N_0 is the central electron density of the bunch and w is the half width of the bunch. The coordinate (x_0, y_0) represents the center of electron-bunch, and its movement (trajectory) is updated by solving following equation of motion:

$$\frac{\partial \boldsymbol{P}(x_0,y_0,t)}{\partial t} = -n_e e\{\boldsymbol{E}(x_0,y_0,t) + \boldsymbol{v}(x_0,y_0,t) \times \boldsymbol{B}(x_0,y_0,t)\} \tag{18}$$

$$\boldsymbol{P}(x_0,y_0,t) = \frac{m_e \boldsymbol{v}(x_0,y_0,t)}{\sqrt{1-|\boldsymbol{v}(x_0,y_0,t)|^2/c^2}} \tag{19}$$

where $\boldsymbol{P}$ is the momentum, e is the electron charge, $\boldsymbol{v}$ is the speed of the electron-bunch, and m_e is the electron mass. The movement of the electron-bunch is assumed to be in a continuous space, and the coordinate (x_0, y_0) of the center position of it is not necessarily on Yee's discrete FDTD grid points. Therefore, electric field and magnetic flux density on the electron-bunch to solve Eq. (18) should be interpolated from those at the nearest grid points. We used linear interpolation as schematically shown in **Figure 3**, in which E_x component is given as follows:

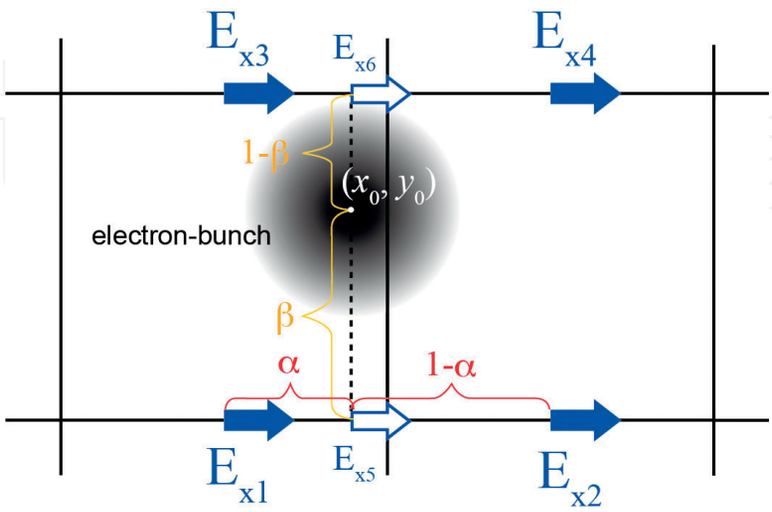

Figure 3. Schematic representation of the linear interpolation for E_x components at the center position (x_0, y_0) of the electron-bunch.

$$E_{x5} = (1-\alpha)E_{x1} + \alpha E_{x2} \tag{20}$$

$$E_{x6} = (1-\alpha)E_{x3} + \alpha E_{x4} \tag{21}$$

$$E_x = (1-\beta)E_{x5} + \beta E_{x6} \tag{22}$$

In order to include the movement of the electron-bunch in the FDTD formalism, a current source term is added to Ampere's law:

$$\boldsymbol{J}(x,y,t) = -n_e(x,y,t)e\boldsymbol{v}(x_0,y_0,t) \tag{23}$$

Figure 4 schematically summarizes our simplified PIC-FDTD simulation scheme. The solution of the time-dependent Maxwell's equations gives spatial counter maps of EM fields and their time evolution. The solution of the equation of motion of relativistic electron-bunch gives its trajectory, and the continuity equation gives the current and charge densities required for Maxwell's equations. The flowchart of our PIC-FDTD simulation is shown in **Figure 5**.

2.2. Analyzed models and parameters

In **Figure 1**, the analyzed 2D system and definitions of dimensions of the graded grating are schematically shown. In **Table 1**, parameters used in this study are summarized. The graded grating was assumed to be consisted of Ag, and the Drude model was adopted in order to model the dispersion characters of its dielectric function and solved by using RC scheme as discussed above. The plasma frequency (ω_p) and the collision frequency (Γ) of Ag were set to

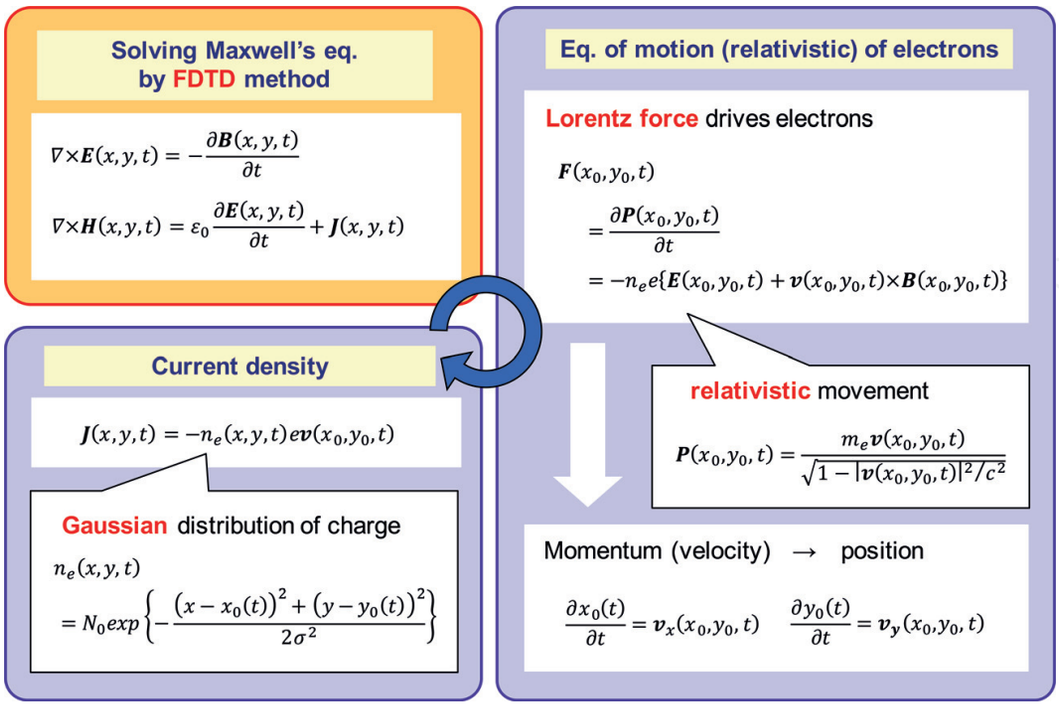

Figure 4. Schematic representation of simplified PIC-FDTD simulation scheme.

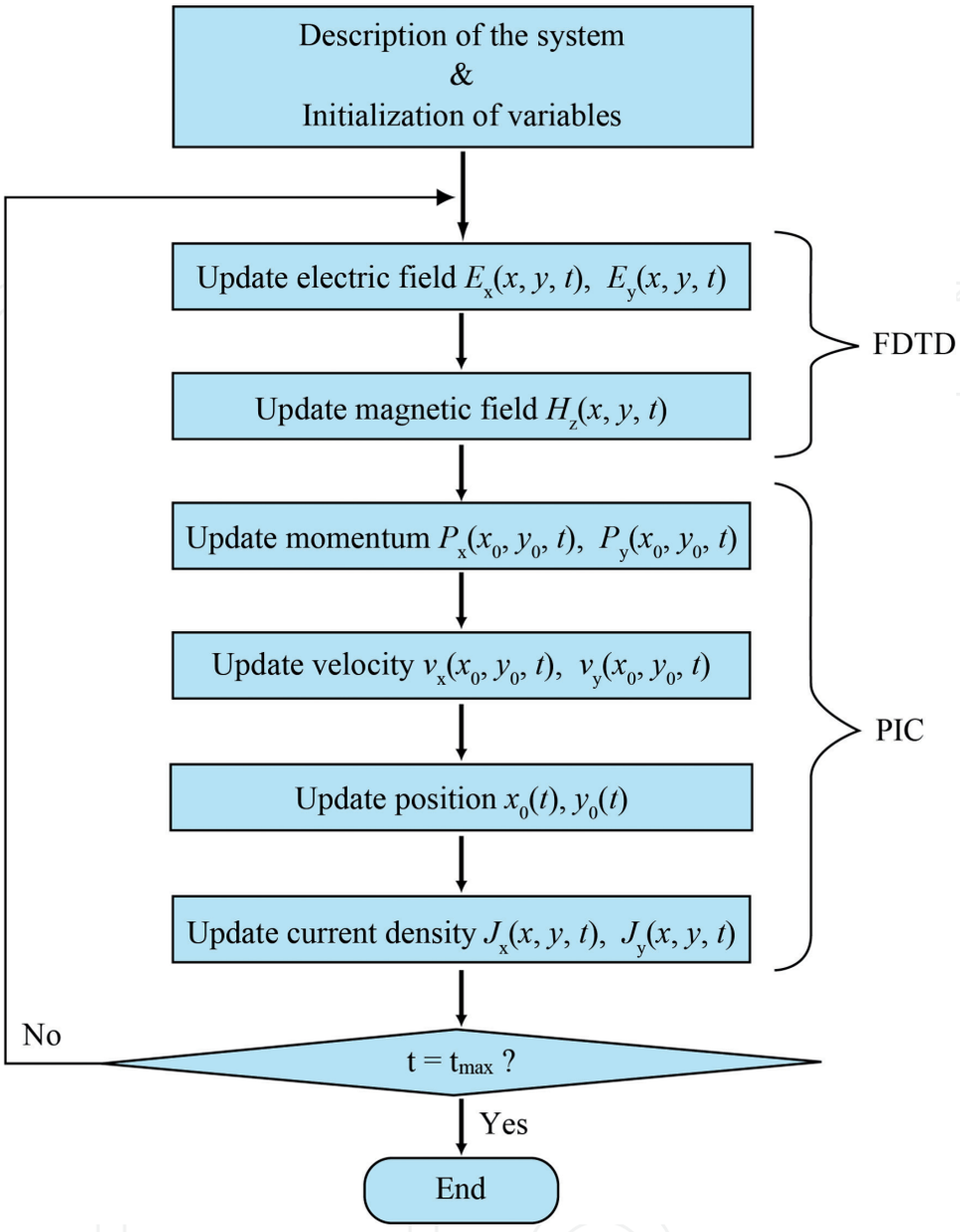

Figure 5. Flowchart of our PIC-FDTD scheme.

be 2.2 × 10^3 and 5.4 THz, respectively. The grating period (Λ) and the groove width (s) are 170 and 60 μm, respectively. The number of grooves of the grating (N) is 35. The groove depth (d) is gradually made deeper or shallower. Here, we denote each graded grating using grating parameters as GG[d_s, d_d, Δd], where d_s and d_d are the shallowest and the deepest groove depths, respectively, and Δd is the difference in depths between two consecutive grooves (all values are in μm). The space increment for the FDTD grids chosen here is $\Delta x = \Delta y = 10$ μm. The time increment is set to be $\Delta t = 23$ fs, which is sufficiently small to satisfy the condition for the stabilization of the FDTD algorithm.

Grating period (Λ)	170 μm
Groove width (s)	60 μm
Groove depth (d)	Variable parameter
Number of grooves (N)	35
Plasma frequency of Ag (ω_p)	2.2×10^3 THz
Collision frequency of Ag (Γ)	5.4 THz
Electron-bunch energy	30 keV
Half width of electron-bunch (w)	20 μm
Bunch-grating distance (w)	20 μm

Table 1. Parameters used in this study.

A 20-μm-wide (w) bunched electron-bunch with Gaussian charge distribution (Eqs. (16) and (17)) was sent 20 μm (w) above the grating at the relativistic speed. The maximum current density at the center of the electron-bunch was assumed to be 1.0×10^6 A/m^2, and the acceleration energy of the electron-bunch is 30 keV, which is comparable to the recent experimental condition by Urata et al. [5].

3. Results and discussions

In the e-beam-induced radiations from conventional periodic grating, there are two mechanisms. One is the so-called Smith-Purcell radiation emitted while the e-beam is passing over the grating. The radiation angle and its frequency satisfy Eq. (1). The other is the scattering of surface waves at both ends of the grating long after the e-beam moved away from the grating. These long-lived surface waves can propagate back and forth on the grating surface and can be emitted repeatedly even long after the e-beam has moved away from the grating as long as the surface waves can live. The frequency of the scattered surface waves is determined by the intersection of the dispersion curves of the surface wave and the beam line. Here, we are interested in the second mechanism long after the e-beam has moved away from the gratings, but the groove depths are gradually graded, and, therefore, the dispersion curves of the surface waves induced by an e-beam cannot be uniquely determined.

Figure 6(a) and **(b)** shows snapshot contour maps of the H_z field long after the e-beam has moved away from the graded grating of GG[100, 168, 2] and GG[100, 168, −2], respectively. In both cases, directional radiations are obtained only from the shallowest end of the graded grating, in backward direction from GG[100, 168, 2] and forward direction from GG[100, 168, −2], respectively. These directional radiation characteristics cannot be expected from a conventional periodic grating and might be unique in the graded grating considered here.

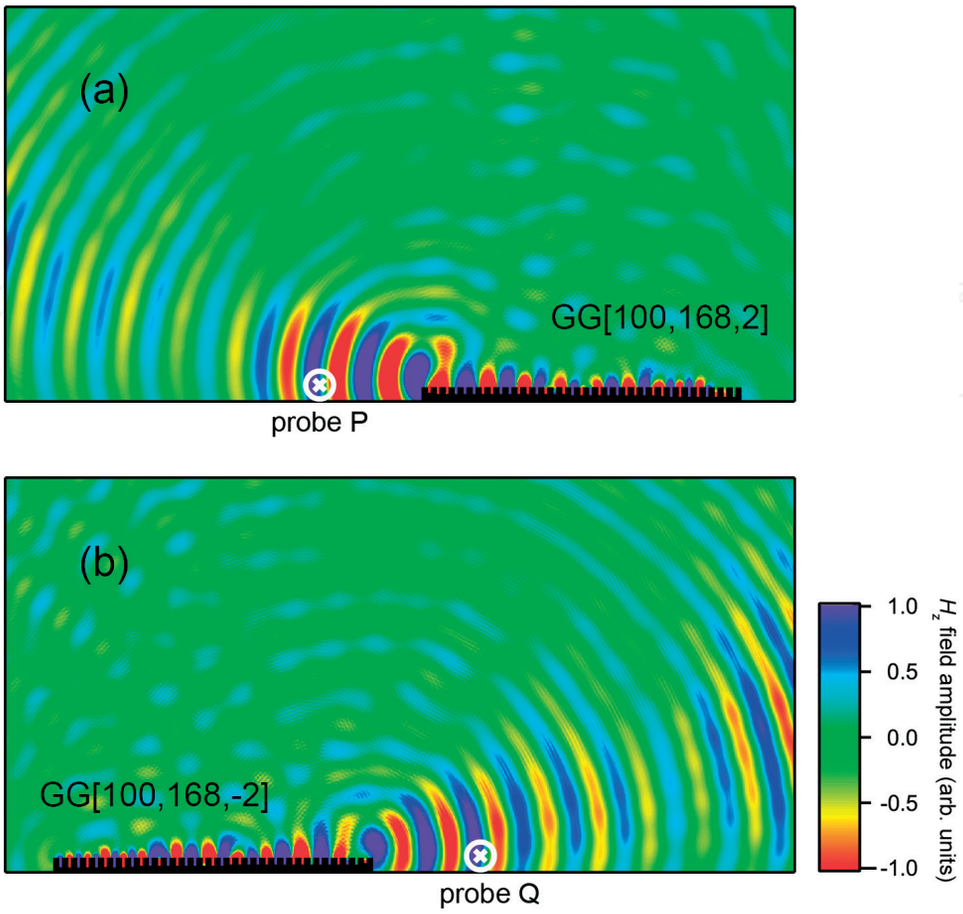

Figure 6. Snapshot contour map of H_z field long after the e-beam moved over (a) GG[100, 168, 2] and (b) GG[100, 168, −2].

As discussed by Gan et al. [16], the dispersion relations of the surface waves on these graded gratings are different at each location on the grating, and thus the frequencies of the e-beam-induced surface waves should also be different at different locations. These surface modes with different frequency components originated from different locations on the graded gratings can propagate toward the side with shallower groove depth due to the cutoff nature as reported by Gan et al. [16], which may give a mechanism of the directional radiation obtained only from the shallow end of the graded grating.

Figure 7(a) shows the time-domain H_z field amplitude from GG[100, 168, 2] monitored at probe P indicated in **Figure 6(a)**. After around 400 ps, successive pulse train with exponentially decaying magnitude can be seen. Magnified figure in the inset of **Figure 7(a)** indicates that each pulse train has duration of tens of ps and seems to be composed by the beating between several frequency components. **Figure 7(b)** shows the Fourier-transformed spectra of the far-field radiation from GG[100, 168, 2] monitored at probe P and from GG[100, 168, −2] monitored at probe Q. Both spectra have relatively wideband spectra and multiple sharp peaks, which cannot be expected from a conventional SPR in a periodic grating. The beating response seen in

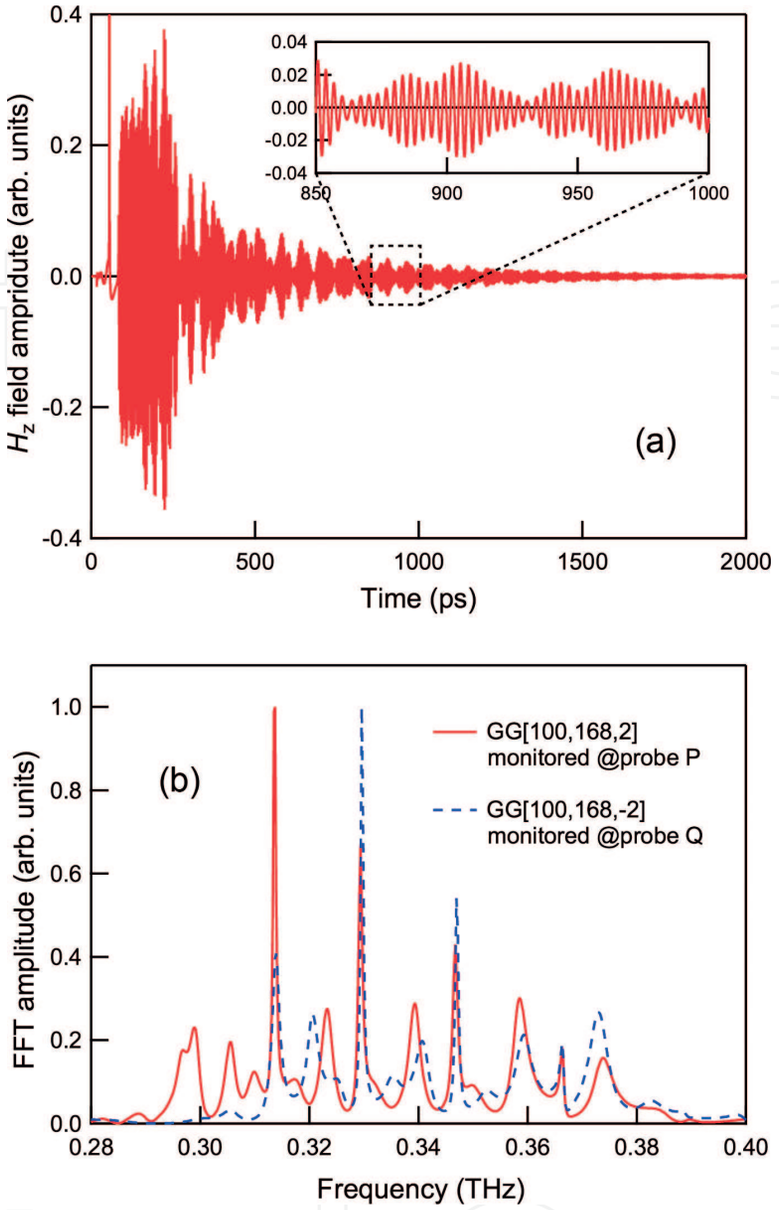

Figure 7. (a) Time-domain H_z field amplitude from GG[100, 168, 2] monitored at probe P. (b) Fourier-transformed spectra of the far-field radiation from GG[100, 168, 2] monitored at probe P (red solid line) and from GG[100, 168, −2] monitored at probe Q (blue-dotted line).

time-domain response in **Figure 7(a)** should be attributed to these multiple sharp peaks. These two spectra from GG[100, 168, 2] and GG[100, 168, −2] are quite similar. The geometric parameters of these two graded gratings are identical except the groove depth variation Δd is opposite in sign; therefore, e-beam-induced surface modes are almost identical in both graded gratings, and only radiation direction was switched by making groove depth variation Δd opposite.

In order to clarify the nature of the surface modes, we have also investigated near fields on the different locations on the graded gratings. **Figure 8** shows Fourier-transformed

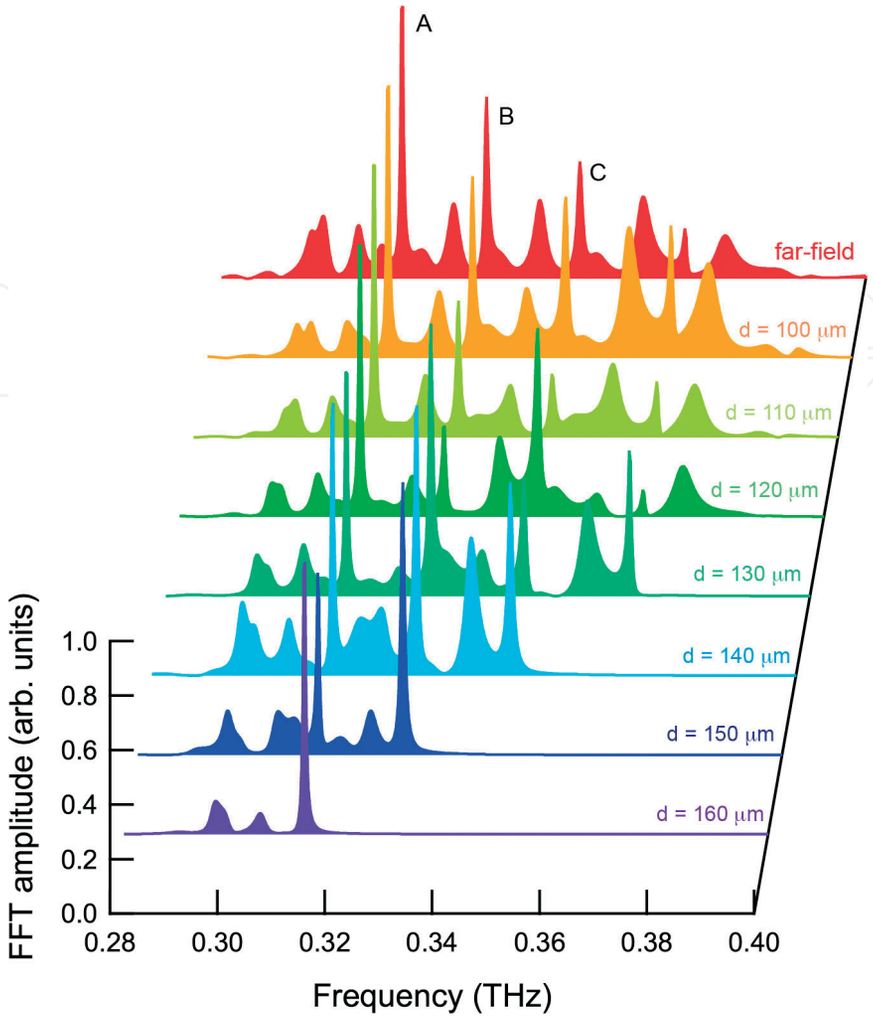

Figure 8. Fourier-transformed spectra of near-field (surface wave) H_z monitored at several positions 10 μm above each groove with depth of d = 160, 150, 140, 130, 120, 110, or 100 μm, along with that of the far-field radiation monitored at the probe P in GG[100, 168, 2] (from top to bottom). Markers A, B, and C refer to the peaks at 0.314, 0.329, and 0.347 THz, respectively.

spectra of the near-field (surface wave) H_z field monitored just above each groove with d = 160, 150, 140, 130, 120, 110, or 100 μm, along with that of the far-field radiation monitored at the probe P, all in GG[100, 168, 2]. It can be seen that more peaks appear on the higher-frequency side of the spectra for monitoring above the shallower grooves. This is because the frequency of the surface waves and their cutoff frequency are lower at deeper grooves, and more surface modes can be supported above the shallower grooves. The spectrum monitored at the left end groove of the grating (d = 100 μm) is almost identical to the far-field radiation spectrum, which also supports that the directional and wideband far-field radiation with multiple sharp peaks was obtained as a superposition of all of the surface modes with different frequencies originated at different locations on the graded grating.

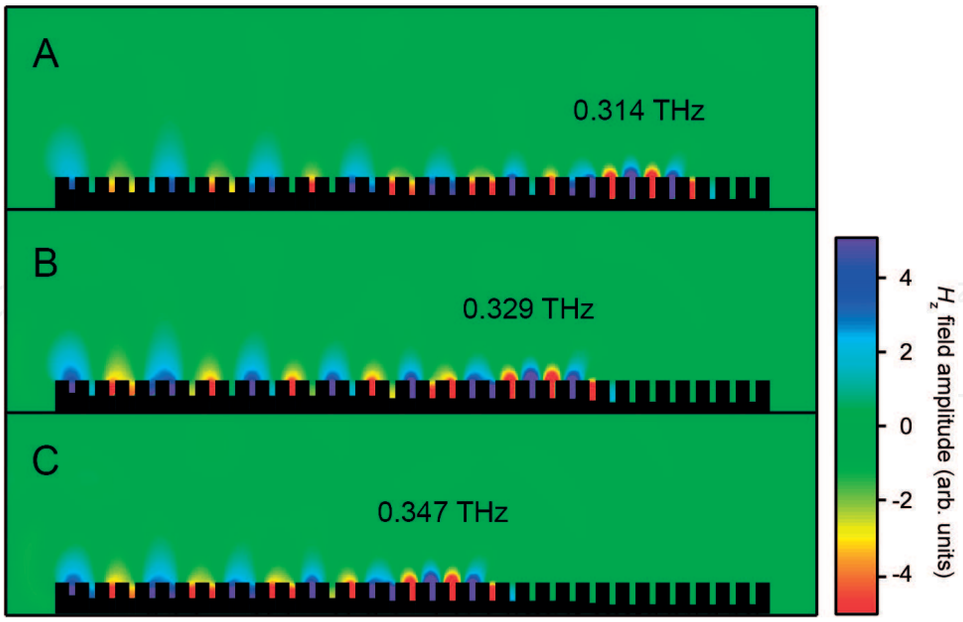

Figure 9. Snapshot contour map of H_z fields long after the exciting quasi-monochromatic electromagnetic pulse has been damped when the frequencies of the mode are 0.314 (A), 0.329 (B), and 0.347 (C) THz in GG[100, 168, 2]. Each mode and its name (A, B, C) correspond to the peaks in the far-field radiation spectrum in **Figure 8**.

In order to reveal from where each mode originate in the graded grating, we excited the system with quasi-monochromatic EM pulse and monitored long enough until the initial pulse damped and only long-lived surface modes survive. **Figure 9** shows spatial distributions of H_z fields for quasi-monochromatic long-lived surface modes of 0.314 (A), 0.329 (B), and 0.347 (C) THz. It can be seen that each surface modes originate at different locations of the graded grating and that higher-frequency modes originate at shallower grooves. This also supports that a superposition of the surface modes with different frequencies originated at different locations on the graded grating results in the directional and wideband far-field radiation with multiple sharp peaks.

The fact that the dispersion characters and frequency of the e-beam-induced surface mode is quite sensitive to the local environment of the grooves suggests that one can design the radiation frequency of the directional radiation from graded gratings by appropriately choosing groove parameters of the grating. **Figure 10** shows the Fourier-transformed spectra of the far-field radiation from graded gratings with different groove parameters: GG[100, 304, 6], GG[100, 236, 4], GG[100, 168, 2], GG[168, 236, 2], GG[50, 186, 4], and GG[50, 118, 2]. Roughly speaking, the deepest and shallowest grooves determine the lowest and highest frequencies of the radiation, respectively. This can be confirmed by comparing spectra for GG[100, 304, 6], GG[100, 236, 4], and GG[100, 168, 2], for example. The highest frequency of these radiations is almost the same ~0.40 THz and determined by their common shallowest groove depth d_s of 100 μm. The concept of spoof SPPs may be promising for developing THz radiation sources.

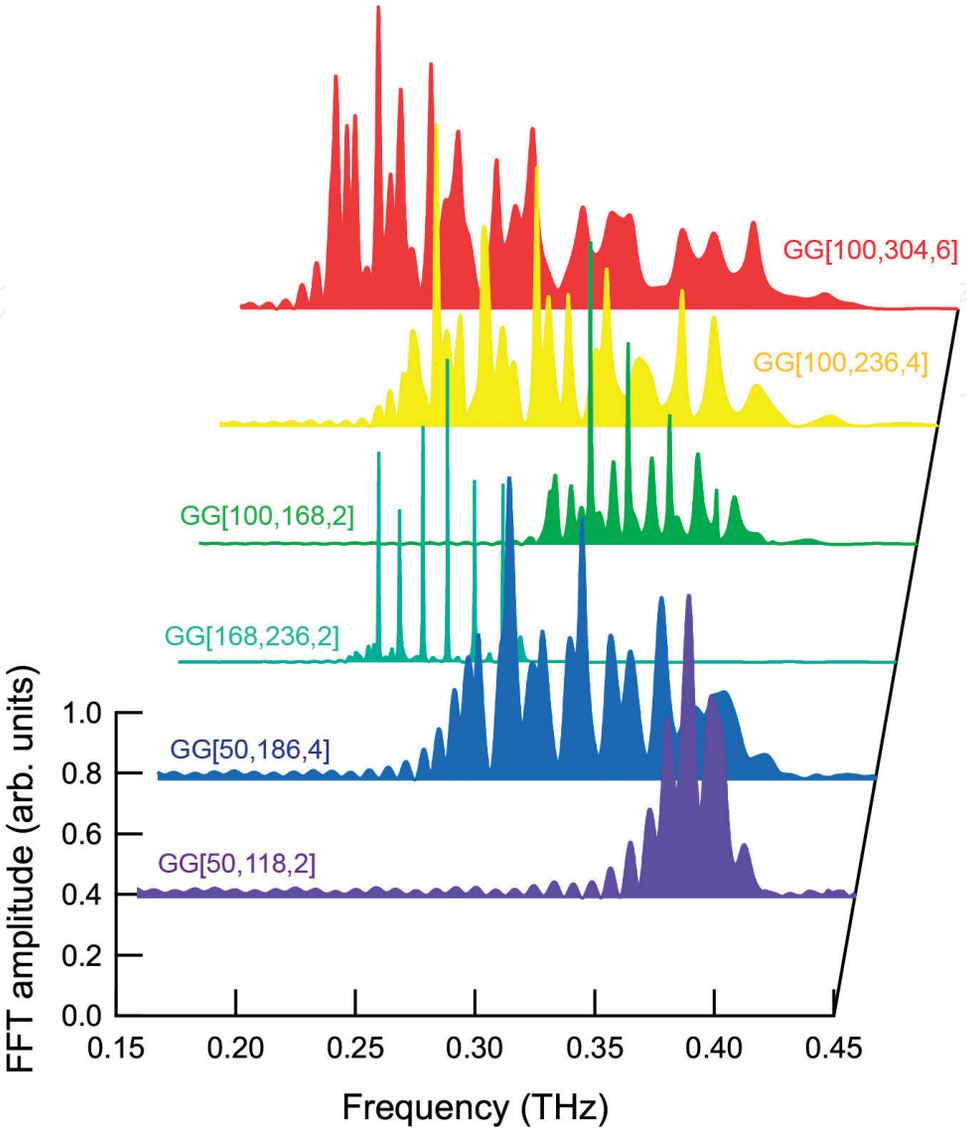

Figure 10. Fourier-transformed spectra of the far-field radiation from graded gratings with different groove parameters: GG[100, 304, 6], GG[100, 236, 4], GG[100, 168, 2], GG[168, 236, 2], GG[50, 186, 4], and GG[50, 118, 2] (from top to bottom).

4. Conclusions

We have numerically analyzed the e-beam-induced directional THz radiation from metallic grating structures with graded depths. We used a simplified PIC-FDTD method for numerical analysis to save computational time and memory, and the detailed description of our method is given here. In our simplified model, the electron-bunch is treated as one negatively charged particle with Gaussian charge distribution, and its movement is restricted only in 2D space, and only TE mode, with E_x, E_y, and H_z fields, has been analyzed.

Our results show unique directional THz radiation from graded gratings. By passing pulsed (bunched) e-beam along the grating surface, directional THz radiations are obtained from one

side of the grating with shallower grooves. The direction of these radiations can be switched backward or forward by making the groove depth deeper or shallower. The spectra of these directional radiations are wideband and contain multiple sharp peaks. The deepest and the shallowest groove depths determine the lowest and the highest frequency of the radiation band, respectively. These unique radiation characteristics cannot be explained by the conventional Smith-Purcell radiation and should be attributed to the spoof SPP that originates from different locations on the graded grating. The unique e-beam-induced radiation from metamaterials based on spoof SPP's concept may open a way for a development of novel types of THz radiation sources.

Acknowledgments

This work is partly supported from Okasan-Kato Foundation. The presented works have been carried out with graduate students who formerly belonged and currently belong to our research group, Okajima, Omura, and Yoshida.

Conflict of interest

There is no conflict of interest.

Author details

Tatsunosuke Matsui

Address all correspondence to: matsui@elec.mie-u.ac.jp

Department of Electrical and Electronic Engineering, Graduate School of Engineering, Mie University, Tsu, Japan

References

[1] Tonouchi M. Cutting-edge terahertz technology. Nature Photonics. 2007;**1**:97-105. DOI: 10.1038/nphoton.2007.3

[2] Hangyo M. Development and future prospects of terahertz technology. Japanese Journal of Applied Physics. 2015;**54**:120101. DOI: 10.7567/JJAP.54.120101

[3] Matsui T. A brief review on metamaterial-based vacuum electronics for terahertz and microwave science and technology. Journal of Infrared, Millimeter and Terahertz Waves. 2017;**38**:1140-1161. DOI: 10.1007/s10762-017-0387-9

[4] Smith SJ, Purcell EM. Visible light from localized surface charges moving across a grating. Physics Review. 1953;**92**:1069. DOI: 10.1103/PhysRev.92.1069

[5] Urata J, Goldstein M, Kimmitt MF, Naumov A, Platt C, Walsh JE. Superradiant Smith–Purcell emission. Physical Review Letters. 1998;**80**:516-519. DOI: 10.1103/PhysRevLett.80.516

[6] Andrews HL, Brau CA. Gain of a Smith-Purcell free-electron laser. Physical Review Accelerators and Beams. 2004;**7**:070701. DOI: 10.1103/PhysRevSTAB. 7.070701

[7] Gover A. Superradiant and stimulated-superradiant emission in prebunched electron-beam radiators. I. Formulation. Physical Review Accelerators and Beams. 2005;**8**:030701. DOI: 10.1103/PhysRevSTAB. 8.030701

[8] Donohue JT, Gardelle J. Simulation of Smith-Purcell radiation using a particle-in-cell code. Physical Review Accelerators and Beams. 2005;**8**:060702. DOI: 10.1103/PhysRevSTAB. 8.060702

[9] Donohue JT, Gardelle J. Simulation of Smith-Purcell terahertz radiation using a particle-in-cell code. Physical Review Accelerators and Beams. 2006;**9**:060701. DOI: 10.1103/PhysRevSTAB. 9.060701

[10] Li D, Yang Z, Imasaki K, Park GS. Particle-in-cell simulation of coherent and superradiant Smith-Purcell radiation. Physical Review Accelerators and Beams. 2006;**9**:040701. DOI: 10.1103/PhysRevSTAB. 9.040701

[11] Shalaev VM. Optical negative-index metamaterials. Nature Photonics. 2007;**1**:41-48. DOI: 10.1038/nphoton.2006.49

[12] Withayachumnankul W, Abbott D. Metamaterials in the terahertz regime. IEEE Photonics Journal. 2009;**1**:99-118. DOI: 10.1109/JPHOT.2009.2026288

[13] Zheludev NI, Kivshar YS. From metamaterials to metadevices. Nature Materials. 2012;**11**: 917-924. DOI: 10.1038/nmat3431

[14] Pendry JB, Martín-Moreno L, Garcia-Vidal FJ. Mimicking surface plasmons with structured surfaces. Science. 2004;**305**:847-848. DOI: 10.1126/science.1098999

[15] Garcia-Vidal FJ, Martin-Moreno L, Pendry JB. Surfaces with holes in them: New plasmonic metamaterials. Pure and Applied Optics. 2005;**7**:S97-S101. DOI: 10.1088/1464-4258/7/2/013

[16] Gan Q, Fu Z, Ding YJ, Bartoli FJ. Ultrawide-bandwidth slow-light system based on THz plasmonic graded metallic grating structures. Physical Review Letters. 2008;**100**:256803. DOI: 10.1103/PhysRevLett.100.256803

[17] Okajima A, Matsui T. Electron-beam induced terahertz radiation from graded metallic grating. Optics Express. 2014;**22**:17490-17496. DOI: 10.1364/OE.22.017490

[18] Taga S, Inafune K, Sano E. Analysis of Smith-Purcell radiation in optical region. Optics Express. 2007;**15**:16222-16229. DOI: 10.1364/OE.15.016222

[19] Yee KS. Numerical solution of initial boundary value problems involving Maxwell's equations in isotropic media. IEEE Transactions on Antennas and Propagation. 1966;**14**: 302-307. DOI: 10.1109/TAP.1966.1138693

[20] Taflove A, Hagness SC. Computational Electrodynamics: The Finite-Difference Time-Domain Method. 3rd ed. Norwood, MA: Artech House; 2005. ISBN 1580538320

[21] Berenger JP. A perfectly matched layer for the absorption of electromagnetic waves. Journal of Computational Physics. 1994;**114**:185-200. DOI: 10.1006/jcph.1994.1159

IntechOpen